Energy Conversion and Management 251 (2022) 114918

Contents lists available at ScienceDirect

Energy Conversion and Management

journal homepage: www.elsevier.com/locate/enconman

Comprehensive analysis of the combustion of low carbon fuels (hydrogen, methane and coke oven gas) in a spark ignition engine through CFD modeling

Rafael Ortiz-Imedio, Alfredo Ortiz, Inmaculada Ortiz *

Chemical and Biomolecular Engineering Department, University of Cantabria, Av. Los Castros 46, Santander 39005, Spain

ARTICLE INFO

Keywords:
Coke oven gas
Hydrogen
Methane
Internal combustion engine
Computational fluid dynamics (CFD)
Energy conversion

ABSTRACT

The use of low carbon fuels (LCFs) in internal combustion engines is a promising alternative to reduce pollution while achieving high performance through the conversion of the high energy content of the fuels into mechanical energy. However, optimizing the engine design requires deep knowledge of the complex phenomena involved in combustion that depend on the operating conditions and the fuel employed. In this work, computational fluid dynamics (CFD) simulation tools have been used to get insight into the performance of a Volkswagen Polo 1.4L port-fuel injection spark ignition engine that has been fueled with three different LCFs, coke oven gas (COG), a gaseous by-product of coke manufacture, H_2 and CH_4. The comparison is made in terms of power, pressure, temperature, heat release, flame growth speed, emissions and volumetric efficiency. Simulations in Ansys® Forte® were validated with experiments at the same operating conditions with optimal spark advance, wide open throttle, a wide range of engine speed (2000–5000 rpm) and air-fuel ratio (λ) between 1 and 2. A sensitivity analysis of spark timing has been added to assess its impact on combustion variables. COG, with intermediate flame growth speed, produced the greatest power values but with lower pressure and temperature values at $\lambda = 1.5$, reducing the emissions of NO and the wall heat transfer. The useful energy released with COG was up to 16.5% and 5.1% higher than CH_4 and H_2, respectively. At richer and leaner mixtures ($\lambda = 1$ and $\lambda = 2$), similar performances were obtained compared to CH_4 and H_2, combining advantages of both pure fuels and widening the λ operation range without abnormal combustion. Therefore, suitable management of the operating conditions maximizes the conversion of the waste stream fuel energy into useful energy while limiting emissions.

1. Introduction

Internal combustion engines (ICEs) have played a key role in the 20th century in transport and electricity generation applications. However, conventional fuels have contributed highly to anthropogenic greenhouse gas emissions (GHG) and atmospheric pollution. To overcome this problem, several works have focused on the use of alternative fuels, which are more environmentally friendly and provide high performance in ICEs. Alcohols (e.g. ethanol, methanol and butanol) and biogas are common alternative fuels studied in spark ignition (SI) and compression ignition (CI) engines, reporting many benefits [1,2]. However, they are usually blended with conventional fuels, gasoline and diesel, respectively, maintaining the dependence on fossil fuels [3-5].

On the other hand, hydrogen and methane are receiving great attention as potential gaseous fuels that can be used in conventional engines after some minor modifications [6-9]. In this way, blends with gasoline are avoided, reducing the employment of high pollutant fossil fuels. H_2 provides combustion with zero emissions of CO_2, CO and hydrocarbons (HCs), as well as high thermal efficiency, high in-cylinder pressure and temperature and a wide range of flammability limits. Nevertheless, NOx emissions and a higher tendency to abnormal combustion limit the air-fuel mixture richness, and therefore, the power generation [10,11]. On the other side, CH_4 has a good knocking resistance with rich airfuel mixtures, providing higher power performance at stoichiometric ratios, and reducing pollutant emissions with respect to conventional fuels [12-15]. In order to combine the advantages of both fuels, mixtures of CH_4 and H_2 have been widely studied in literature [16-19]. For instance, in the research of Ma et al. [20], employing mixtures up to 50% of H_2 and operating at fixed ignition timing, higher H_2 content increased NOx emissions and similar thermal efficiency at rich air-fuel ratios were achieved. However, if optimum spark advance (SA) was

* Corresponding author.
E-mail address: ortizi@unican.es (I. Ortiz).

https://doi.org/10.1016/j.enconman.2021.114918
Received 7 July 2021; Received in revised form 19 October 2021; Accepted 20 October 2021
Available online 6 November 2021

Nomenclature

AHRR	apparent heat release rate (J/CAD)
BMEP	brake mean effective pressure (bar)
BSEC	brake specific energy consumption (MJ/kWh)
BSFC	brake specific fuel consumption (g/kWh)
CAD	crank angle degree
CI	compression ignition
CFD	computational fluid dynamics
CHR	chemical heat release (J)
COG	coke oven gas
CR	compression ratio
dABDC	degrees after bottom dead center
dATDC	degrees after top dead center
dBBDC	degrees before bottom dead center
dBTDC	degrees before top dead center
DI	direct injection
EOI	end of injection
EVC	exhaust valve closure
EVO	exhaust valve opening
GHG	greenhouse gas emissions
HCs	hydrocarbons
HCCI	homogeneous charge compression ignition
ICE	internal combustion engine
IVC	intake valve closure
IVO	intake valve opening
LCFs	low carbon fuels
LHV	lower heating value
MBT	maximum brake torque
NG	natural gas
PFI	port-fuel injection
PW	pulse width
RANS	Reynolds-Averaged-Navier-Stokes
RNG	Re-Normalization Group
SA	spark advance
SI	spark ignition
S_L	laminar flame speed
SOI	start of injection
TDC	top dead center
WHT	wall heat transfer (J)
WOT	wide open throttle
A	injection area (m^2)
λ	air-fuel ratio
$\dot{m}$	mass flow rate (g/s)
η_v	volumetric efficiency
η_m	mechanical efficiency
η_t	thermal efficiency
ρ	fuel density (g/m^3)
σ_w	weighted standard deviation
v	injection velocity (m/s)

Table 1
Composition of coke oven gas (COG) in vol% and wt% used in this study.

Composition	H_2	CH_4	CO	N_2	CO_2
vol%	57	30	6	5	2
wt%	11.6	48.5	16.9	14.1	8.9

Table 2
Typical physicochemical properties of H_2, CH_4 and COG calculated at 273.15 K and 10^5 Pa [23].

Gas	H_2	CH_4	COG
LHV (MJ/kg)	120.00 [27]	50.00 [27]	39.86
LHV (kJ/mol)	241.91	802.12	395.50
LHV (MJ/m^3)	9.92	32.91	16.23
Density (kg/m^3) at STP	0.08	0.66	0.41
Molecular weight (g/mol)	2.02 [27]	16.04 [27]	9.92
Stoichiometric ratio (λ_{st})	34.21	17.20	12.72
Flammability range (vol %)	4.0–75.0 [28]	5.3–15.0 [28]	4.4–34.0 [29]
Laminar flame speed (m/s)	2.65–3.25 [30]	0.38 [30]	0.68–0.88 [31,32]

STP means standard temperature (273.15 K) and pressure conditions (10^5 Pa) according to IUPAC [33].

selected, the NOx emissions with rich H_2 mixtures decreased and high thermal efficiency was obtained [20]. Park et al. [15] observed that by raising the H_2 percentage in the mixture up to 40%, the thermal efficiency increased and the specific emissions (g/kWh) were reduced.

As addition to the list of cleaner fuels, industrial waste streams with high percentages of H_2 and CH_4 in their composition, as in the case of clean coke oven gas (COG), are worth considering to harness their energy content [21]. COG is a by-product of coke manufacture, which is a very important good as a reducing agent in the steel industry for producing hot metals from materials that contain iron [22]. The COG is previously processed to extract other valuable components before being used as fuel or to enrich the calorific value of other process gases [22]. Furthermore, this gas is produced at a high volumetric flow rate (280–450 Nm^3/h [22]) per ton of coke, providing a valuable fuel source for stationary ICEs at the outlet of the industrial plant where it is produced in the cases of surplus generation. The typical composition of COG is shown in Table 1 and the main properties of the three fuels are listed in Table 2 [23]. As can be observed, cleaned COG is characterized by a very good composition with high volumetric percentages of H_2 and CH_4 and some other minor gases, generating a process gas with high calorific energy content [22].

Experiments with COG as fuel in ICEs have been carried out in previous works [24-26] and the performance and emissions have been compared to engines fueled with pure H_2 and pure CH_4 [23]. COG combines the advantages of both H_2 and CH_4, improving the performance of H_2 and reducing the emissions of CH_4. In addition, COG offers a wider range of air-fuel ratio (λ), which enables the optimization of the operation point according to the application [23].

Several studies have used CFD software to assess SI ICEs with different configurations and fuels, reducing the experimental effort and expenditures. Hydrogen has been widely studied as combustion fuel using CFD models in direct injection (DI) [34-36] and port-fuel injection (PFI) locations [10,37-39]. Besides the analysis of the performance and emissions, the start of injection (SOI) has been studied to reduce the residual H_2 in the intake manifold and to avoid backfire in PFI engines [40-43]. Generally, temperature, OH mass and NOx emissions distribution in the cylinder are the main variables plotted in 3D graphs. Regarding the kinetics of combustion reactions, the mechanisms more widely employed in literature are Gri-Mech, a detailed mechanism optimized for combustion of natural gas, or reduced mechanisms focused on H_2 combustion reactions [35,44,45].

On the other hand, CH_4 or natural gas (NG) CFD models have been carried out in dual fuel diesel engines [46-48], homogeneous charge compression ignition (HCCI) [49,50] and in SI engines [51-53], analyzing pressure, temperature, emissions and the influence of injection [43]. Mixtures of H_2 and CH_4 gaseous fuels have been also studied through CFD models, analyzing different percentages of H_2 in the

Table 3
Specifications of the original engine (adapted from [61]).

Base vehicle	Volkswagen Polo 1.4
Type	Spark Ignition
Fuel	Gasoline 95 NO
Cylinder line/head material	Aluminum
Number of cylinders	4 in line
Bore/Stroke (mm)	76.5/75.6
Swept volume (cm^3)	1390
Compression ratio	10.5:1
Valve train configuration	DOHC
Number of valves per cylinder	4
Fuel injection system	Port-injection
Ignition system	Single spark ignition coil
Maximum brake power	59 kW at 5000 rpm
Maximum brake torque	132 Nm at 3800 rpm

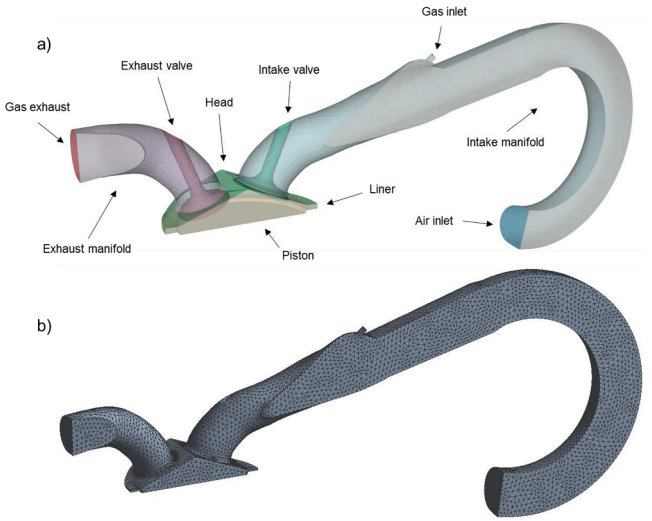

Fig. 1. 3D symmetrical a) geometry model and b) meshing of a single cylinder from the engine. (Screenshots used courtesy of ANSYS, Inc.) .

Table 4
Boundary geometries and conditions.

Boundary region	Boundary type	Condition	Value
Air inlet	Inlet	2000 rpm	0.092 MPa, 314 K
		3000 rpm	0.091 MPa, 311 K
		4000 rpm	0.089 MPa, 309 K
		5000 rpm	0.088 MPa, 307 K
Gas inlet	Inlet		298 K
Gas exhaust	Outlet		0.101 MPa
Intake manifold	No moving wall		313 K
Exhaust manifold	No moving wall		500 K
Head	No moving wall		400 K
Liner	No moving wall		400 K
Piston	Moving wall		500 K
Intake valve	Moving wall	IVO (18.2 dBTDC)	400 K
		IVC (15.2 dABDC)	
Exhaust valve	Moving wall	EVO (19.4 dBBDC)	550 K
		EVC (16.4 dATDC)	

composition [54-57]. Different air-fuel ratios at a single engine speed were considered in order to study the main combustion and performance variables, such as pressure, temperature, rate of heat release, combustion duration, efficiency, flow velocity and emissions. Moreover, two compression ratios (CR) and two engine speeds at different loads were compared in Laget et al. [58].

Regarding COG and syngas with high volumetric H_2 percentages, there are only a few studies with CFD models. He et al. conducted a study focused on the reduction and optimization of the kinetic mechanism of COG combustion [59]. This mechanism was employed in a CFD model in the KIVA-CHEMKIN software of a cylinder from a SI engine. The model was validated with experiments in terms of in-cylinder pressure and NO emissions, showing good agreement between simulated and experimental data. On the other hand, Stylianidis et al. [60] developed a new combustion mechanism for syngas mixtures together with the kinetics of the reactions. However, a modification in the rate constants of the reaction $H_2O_2 + H = H_2 + HO_2$ was needed to improve the match between simulated and experimental data in the case of fuels with high H_2 concentration, as in the case of coke oven feedstock [60]. The authors compared the results obtained with the new chemical kinetic mechanism with previous mechanisms reported for syngas and validated the CFD model in a micro-pilot ignited supercharged dual fuel diesel engine. Results showed good agreement in the evolution of in-cylinder pressure and rate of heat release at different syngas compositions, equivalence ratio and SOI angles.

In consequence, a comprehensive analysis aimed to provide a deeper understanding of the performance of the combustion of COG compared with its main components (H_2 and CH_4) in a SI engine through CFD is still unaccomplished. Therefore, in this work simulations of H_2, CH_4 and COG in a port-fuel cylinder from a Volkswagen Polo 1.4L engine have been carried out matching the experimental operating conditions reported in a previous work [23]. The engine has been run at wide open throttle (WOT) and the spark advance has been selected to achieve the maximum brake torque (MBT). Variations in engine speed between 2000 rpm and 5000 rpm and air-fuel ratio between 1 and 2 have been considered. The model validation has been carried out with different variables. Afterward, the performance assessment in terms of power, heat release, pressure, temperature, flame growth speed, OH concentration and, NO emissions is provided in this work. In addition, the volumetric efficiency has been compared to observe the effects of the different fuel characteristics. Finally, a spark advance sensitivity analysis has been carried out for COG to analyze the impact of this variable on combustion and support the arguments exposed.

2. Simulation methodology

2.1. CFD software

A CFD model of a cylinder from a naturally-aspirated four-cylinder port-fuel injection SI engine has been developed. The original engine is a Volkswagen Polo 1.4L adapted to be driven with gaseous fuels [61]. Specifications of the original engine are detailed in Table 3, extracted from Sopena et al. [61]. Experimental measurements of air-fuel ratio were obtained with an error of ± 0.7% for values close to stoichiometric conditions ($\lambda = 1$) and below ± 3.0% for lean mixtures ($\lambda > 1.7$). Precisions for torque and engine speed were ± 0.2% and ± 1 rpm, respectively. Regarding emissions, measurement deviations in the exhaust gases were ± 0.1% for CO_2, ±0.001% for CO, ±2 ppm for HC and ± 2 ppm for NOx [23]. Therefore, high precision experimental values were achieved during the experiments with an experimental reproducibility higher than the cumulative error from the equipment.

The geometry of a symmetrical cylinder with the intake and exhaust valves and manifolds (Fig. 1a) was designed with Autodesk® Inventor 2020 and exported to Ansys® Academic Research Workbench, Release 2019 R3. This geometry was processed with the packages Ansys® SpaceClaim® and Mesh® to redefine the boundary walls and to create the initial computational mesh, as shown in Fig. 1b. A mesh size sensitivity analysis was carried out and has been included in the Supplementary Material (Table S3), selecting a global element size of 2.5 mm with very good results and reasonable fluid cells number and computational time. However, the average cell size of valve seats and the injector area was reduced to 1.5 mm and 0.5 mm, respectively, to improve the calculation accuracy in those regions with high flow speed and very small contact distance. The initial statistical number of elements generated was around 170,000 cells. Afterward, the model was

Table 5
Simulation planning and injection specifications at each operating condition.

Fuel	λ	Engine Speed (rpm)	Spark advance (CAD)	Injection pressure (bar); velocity (m/s)	Pulse width (CAD)	EOI (CAD)
H_2	1.5	2000	10	3; 275	93	485
		3000	10		150	490
		4000	15		216	495
		5000	15		278	500
	2	2000	25		76	485
		3000	25		120	490
		4000	25		179	495
		5000	25		225	500
CH_4	1	2000	25	3; 115	96	480
		3000	30		149	485
		4000	30		230	490
		5000	30		284	495
	1.5	2000	45		69	485
		3000	60		107	490
		4000	60		164	495
		5000	60		201	500
COG	1	2000	15	4; 113	145	480
		3000	15		228	485
		4000	20		346	490
	1.5	2000	25	3; 150	121	495
		3000	25		191	490
		4000	25		288	495
		5000	25	4; 113	310	500
	2	2000	40	3; 150	97	485
		3000	45		152	490
		4000	45		226	495
		5000	45		282	500

handled in the package Ansys® Forte®, which is a special module focused on ICEs using proven mathematical techniques and algorithms and automatically generating the moving volume mesh on-the-fly during the simulation [62].

Due to the symmetrical position of the hydrogen injector and the unthrottled operation, a symmetrical flow field was assumed without swirl [34]. The vertical plane through the injector's central axis was defined as a symmetry plane, reducing the computational domain and time effort for each simulation. Thus, a high number of simulations could be carried out without significant loss in results accuracy.

Regarding the engine geometry, the boundary conditions of the model are detailed in Table 4. Piston and valves were configured as moving parts, defining the stroke, the connecting rod length and the direction of displacement for the former and the profile movement and direction for each of the valves. All walls were set up with the Law of the Wall slip condition for the shear stress, implying a flexible mesh size near them, and with constant wall temperatures. The air and the gaseous fuel entered in the domain through Inlet surfaces type and the exhaust gas left the domain through an Outlet surface. In the case of the fuel, the Inlet surface was settled in the place of the original place of the port-fuel gasoline injector as a circular area with a diameter of 3.4 mm. Fuel was introduced at a constant injection speed (m/s) during a variable pulse width (PW), which depended on the gas and the operating condition.

The simulation domain can be divided into three regions: intake manifold, cylinder and exhaust manifold. Each of these regions was initialized with a gas composition, pressure and temperature values. The spark timings selected are shown in Table 5 with a duration of 1 ms and an Energy Release Rate of 20 J/s.

Finally, some mesh refinements were added in Ansys® Forte® for the walls, the symmetry plane, the open boundaries, inside the cylinder and near the valves to increase precision in the calculation in the regions with higher flow velocity gradients and heat transfer. The resulting average cell size inside the cylinder is of 1.25 mm. However, a variable mesh during the spark ignition in the spark region and in the squish periods within the cylinder was applied to improve combustion calculations [63]. Furthermore, a solution adaptive mesh refinement for temperature was added within the cylinder based on the gradient of the temperature field from the spark time to the EVO. Both refinements enable a reduction of the average cell size to 0.625 mm in the region and periods of time with higher calculation requirements.

Several chemical kinetic mechanisms have been found in the literature for simulation of the combustion of hydrogen, methane and mixtures of fuels. These mechanisms define the reaction pathways and the evolution of the reaction rates during combustion, leading to changes in species concentration. In order to compare the three gaseous fuels under the same simulation conditions, the detailed Gri-Mech 3.0 mechanism with 325 reactions and 53 species, was selected to consider all the hydrogen and hydrocarbon reactions as well as the NOx emissions [64].

The turbulent flow model used in this study was the Reynolds-Averaged-Navier-Stokes (RANS) Re-Normalization Group (RNG) k-ε model, aiming to capture the average of the entire flow field while preserving the main effects of turbulence on the averaged flow and combustion characteristics [63]. Furthermore, the RNG k-ε model is the default and recommended turbulence model in Ansys® Forte® with better engine simulation results compared to the standard version of the k-ε model [65]. On the other hand, the Table Library included in Forte with prebuilt laminar flame speeds has been employed for the gaseous fuels [76]. These built-in flame speed values cover a wide range of operating conditions and is the recommended option by the software support.

The calculations were performed with MPI solver in a workstation with two processors Intel® Xeon® Gold 6148 and 256 GB RAM and in the supercomputer Altamira Supercomputer at the Institute of Physics of Cantabria (IFCA-CSIC). Simulations of at least four consecutive cycles have been done for each study case to reach a quasi-steady state, requiring between 30 and 45 h for the calculation of four cycles with 16 cores.

2.2. Planning of simulation runs

The simulations carried out in this work were based on the experiments of H_2, CH_4 and COG performed in a previous investigation [23]. Engine speed was varied in the range 2000 rpm – 5000 rpm and the air-fuel ratio between 1 and 2. In addition, full load (WOT) and optimum spark advance were selected to obtain maximum brake torque. Spark advance is defined as crank angle degrees (CAD) before top dead center (TDC), which is "720" in this work.

Gaseous fuels were injected using a time-varying velocity profile according to the density and specification of mass flow rate of the injectors (Quantum PQ2-3200). The injection velocity, v in m/s, was calculated with Eq. (1):

$$v = \frac{\dot{m}}{\rho \cdot A} \tag{1}$$

Where $\dot{m}$is the mass flow rate (g/s), ρ is the fuel density (g/m^3) and A is the injection area (m^2). The resulting half of the injection area due to the symmetrical part of the CFD geometry model is approximately 4.5 mm^2, calculated with the gas nozzle diameter (3.4 mm). Density of each fuel was assumed at 3 bar and 298 K as it was the injection pressure employed in the experiments [23]. Injection mass flow rates of H_2, COG and CH_4 at 3 bar are 0.6 g/s, 1.4 g/s and 2 g/s, respectively. However, in the case of simulations of COG at $\lambda = 1$ and in the case of $\lambda = 1.5$ at 5000 rpm, density was calculated at 4 bar and 298 K, as the injection pressure was increased during the experiments, with an injection mass flow rate of 1.62 g/s. As the symmetry plane of the geometry divides the injection area to the half, the mass flow rates were also halved for the calculation of the injection velocity.

The end of injection (EOI) CAD for each engine speed and air-fuel ratio were selected following the recommendations of Liu et al. [40] (Table 5). In this way, enough time was provided for the gas to enter in the cylinder due to the travel distance from the injector to the intake valves [66]. Therefore, the accumulation of the gas in the intake

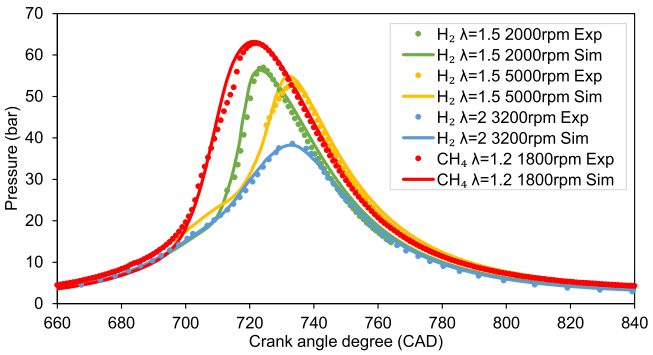

Fig. 2. Experimental (dots) and simulated (lines) results of in-cylinder pressure (bar) for H_2 at λ = 1.5 (2000 rpm and 5000 rpm) and at λ = 2 (3200 rpm) and CH_4 at λ = 1.5 and 1800 rpm versus the crank angle degree (CAD) [10,77].

manifold was reduced during subsequent cycles, diminishing the possibility of backfire. Finally, the pulse width was adjusted to achieve the desired λ value.

Finally, as the software provides the "indicated" values inside the cylinder, to obtain comparable results with the experiments ("brake" values), a mechanical efficiency (η_m) correlation was applied, only dependent on engine speed [67]. The maximum η_m was assumed to be 90% at 2000 rpm, decreasing linearly to 75% at 5000 rpm [27].

3. Results

The simulation results will be exposed in this section starting with the engine performance in terms of output power and heat released in the simulated fourth cycle. In addition, the evolution of some variables inside the cylinder are graphed, such as pressure, temperature, apparent heat release rate (AHRR) and mass fraction of OH and NO. Afterward, the fluid dynamics in terms of volumetric efficiency and mass flow rates and mass exchanges between the cylinder and the manifolds are studied. Finally, a sensitivity analysis of the spark advance with one of the gases, COG, is carried out to observe the influence of this variable in the engine performance.

3.1. Engine performance

The simulation model has been validated with experiments of H_2, CH_4 and COG carried out in a previous work at the same operating conditions [23].

The simulated in-cylinder pressure has been validated with experimental results, demonstrating the good match between model predictions and experimental performance. The average in-cylinder pressure curves for H_2 at different engine speeds and air-fuel ratios are shown in Fig. 2. Peak pressure relative errors of 3.37%, 1.08% and 0.88% are obtained for 2000 rpm, 5000 rpm and 3200 rpm cases, respectively. In addition, the pressure evolution inside the cylinder for CH_4 at 1800 rpm is also graphed in Fig. 2, with a peak pressure relative error of 0.65%. Therefore, this good agreement makes the model very reliable in the in-cylinder pressure variable. Regarding the air-fuel ratio trend, the employment of leaner mixtures (λ = 2) reduces the pressure within the cylinder. In addition, the role of spark advance is highly apparent, increasing the maximum pressure of the 2000 rpm over the 5000 rpm curve due to the higher spark advance in the case of H_2, and even higher pressure with CH_4 with an earlier spark ignition timing.

In addition, validation results between experiments and simulations are provided in Appendix A with a parity graph of the brake mean effective pressure (BMEP) and brake specific fuel consumption (BSFC) in Fig. A1. A bar graph comparing the experimental and simulated CO_2 emissions in %vol has been also plotted in Fig. A2. Furthermore, the weighted standard deviation (σ_w) statistical parameter for the performance variables (Table A1) has been provided. A good agreement can be noticed, with a deviation lower than 12% for power and BMEP, 14.2% for BSFC and brake specific energy consumption (BSEC) and up to 16.3% for the thermal efficiency (η_t).

The experimental and simulated brake power of H_2, CH_4 and COG are graphed in Fig. 3. The good agreement between experiments and simulations is observed. Furthermore, the total chemical heat release (CHR) and total wall heat transfer (WHT), two variables directly related to power, of COG, CH_4 and H_2 are graphed at different λ values in Fig. 4. Both variables are calculated by the software Ansys Forte® inside the cylinder. The CHR (J) is defined as the accumulation of the heat release from the combustion chemical reactions, remaining constant once the combustion is completed. On the other hand, the WHT (J) is obtained as the accumulation of heat transfer loss through the walls of the cylinder, varying along the cycle. Therefore, the CHR and the WHT values have been evaluated at EVO before the exhaust process is carried out, and subtracting the heat releases from the previous cycles. The combustion stages from the simulations for all the gases and operational conditions are explained and collected in Table S1 in the Supplementary Material.

As can be observed in Fig. 3, the most important factor is the air-fuel ratio, increasing the delivered power as the mixture becomes richer (lower λ), obtaining higher CHR, pressure and temperature. Nevertheless, the WHT through the walls also increases as the mixture becomes richer (Fig. 4). This effect is attenuated in the case of WHT at high engine speeds for CH_4 because very high spark advances at λ = 1.5 produce high heat losses [68].

In the case of λ = 1 (Fig. 3a), COG and CH_4 provide very similar brake power values because both fuels produce high CHR and WHT, resulting in a low performance difference (Fig. 4a). At intermediate air-fuel ratio (λ = 1.5, Fig. 3b), COG provides the highest power values as a result

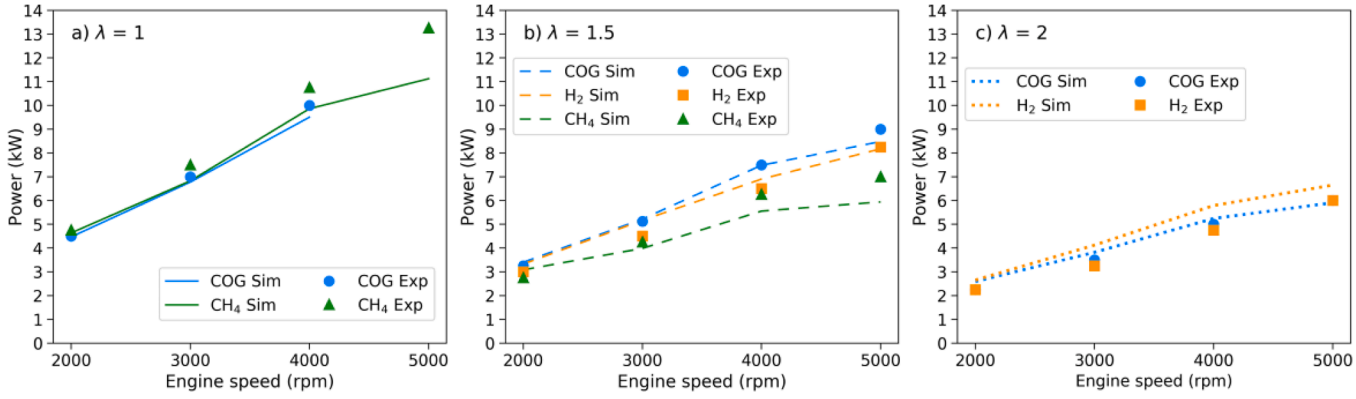

Fig. 3. Simulated (lines) and experimental (discrete values) brake power (kW) of H_2 (orange squares), CH_4 (green triangles) and COG (blue dots) versus engine speed at a) λ = 1 (solid), b) λ = 1.5 (dashed) and c) λ = 2 (dotted lines).

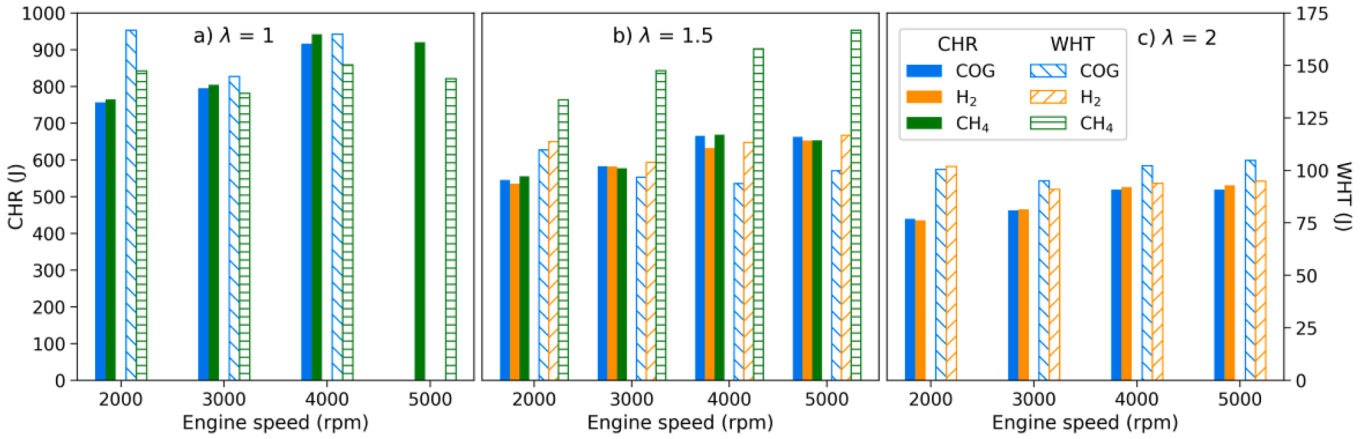

Fig. 4. CHR (solid bars) and WHT (dashed bars) of COG (blue), CH_4 (green) and H_2 (orange) versus engine speed at a) $\lambda = 1$, b) $\lambda = 1.5$ and c) $\lambda = 2$. (For interpretation of the references to colour in this figure legend, the reader is referred to the web version of this article.)

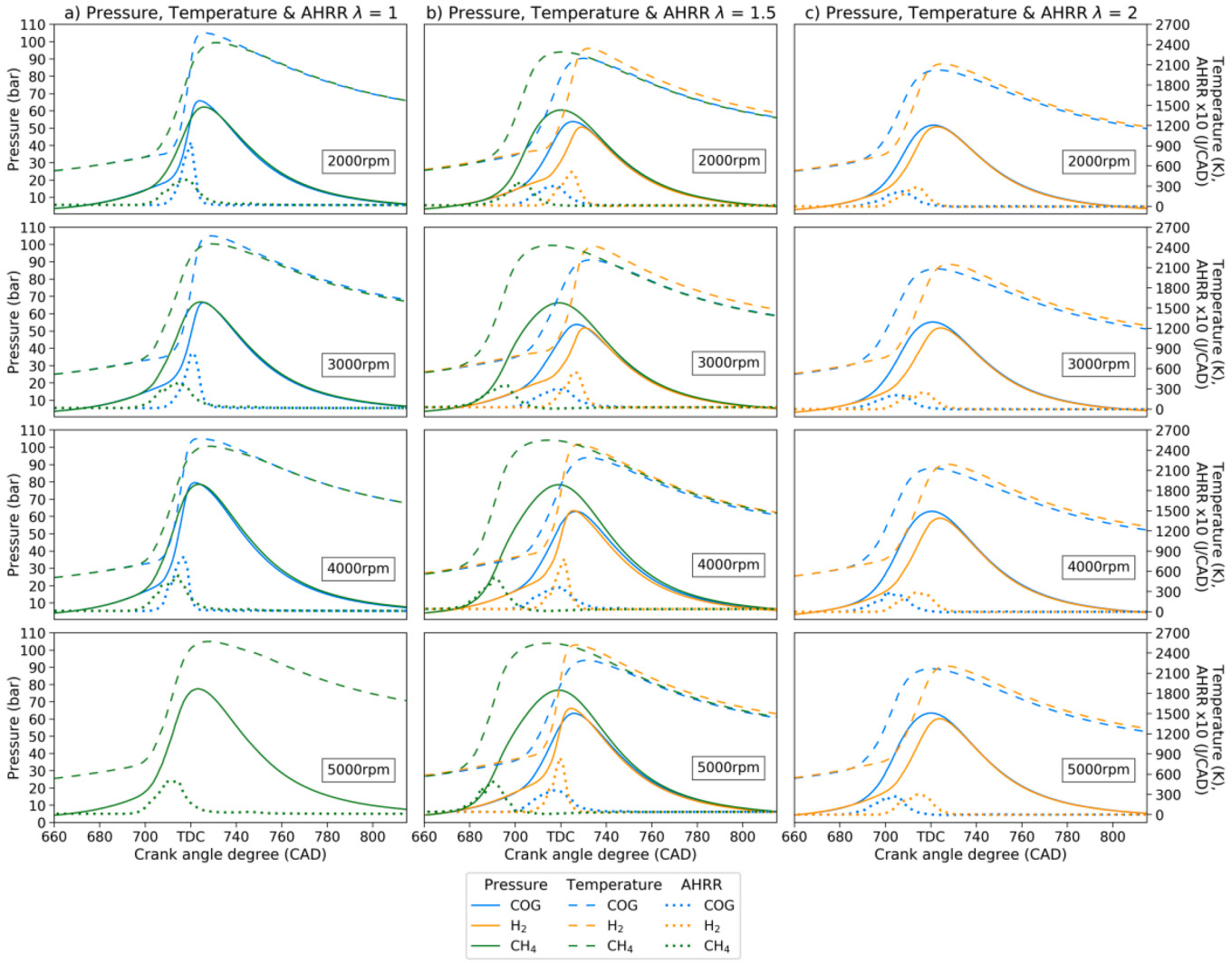

Fig. 5. Pressure (solid lines), temperature (dashed lines) and AHRR (represented 10 times higher and with dotted lines) inside the cylinder at a) $\lambda = 1$, b) $\lambda = 1.5$ and c) $\lambda = 2$ for H_2 (orange), CH_4 (green) and COG (blue) gaseous fuels in the entire speed range. (For interpretation of the references to colour in this figure legend, the reader is referred to the web version of this article.)

from a higher laminar speed (S_L) than CH_4 and a higher volumetric lower heating value (LHV) (16.23 MJ/m^3) than H_2 (9.92 MJ/m^3) (see Table 2) [23]. As can be observed in Fig. 4b, COG delivers similar CHR but with the lowest WHT values at $\lambda = 1.5$ due to a lower value of the maximum temperature, which increases the difference in brake power with respect to H_2 and CH_4. At 5000 rpm, COG releases 40.1% of WHT

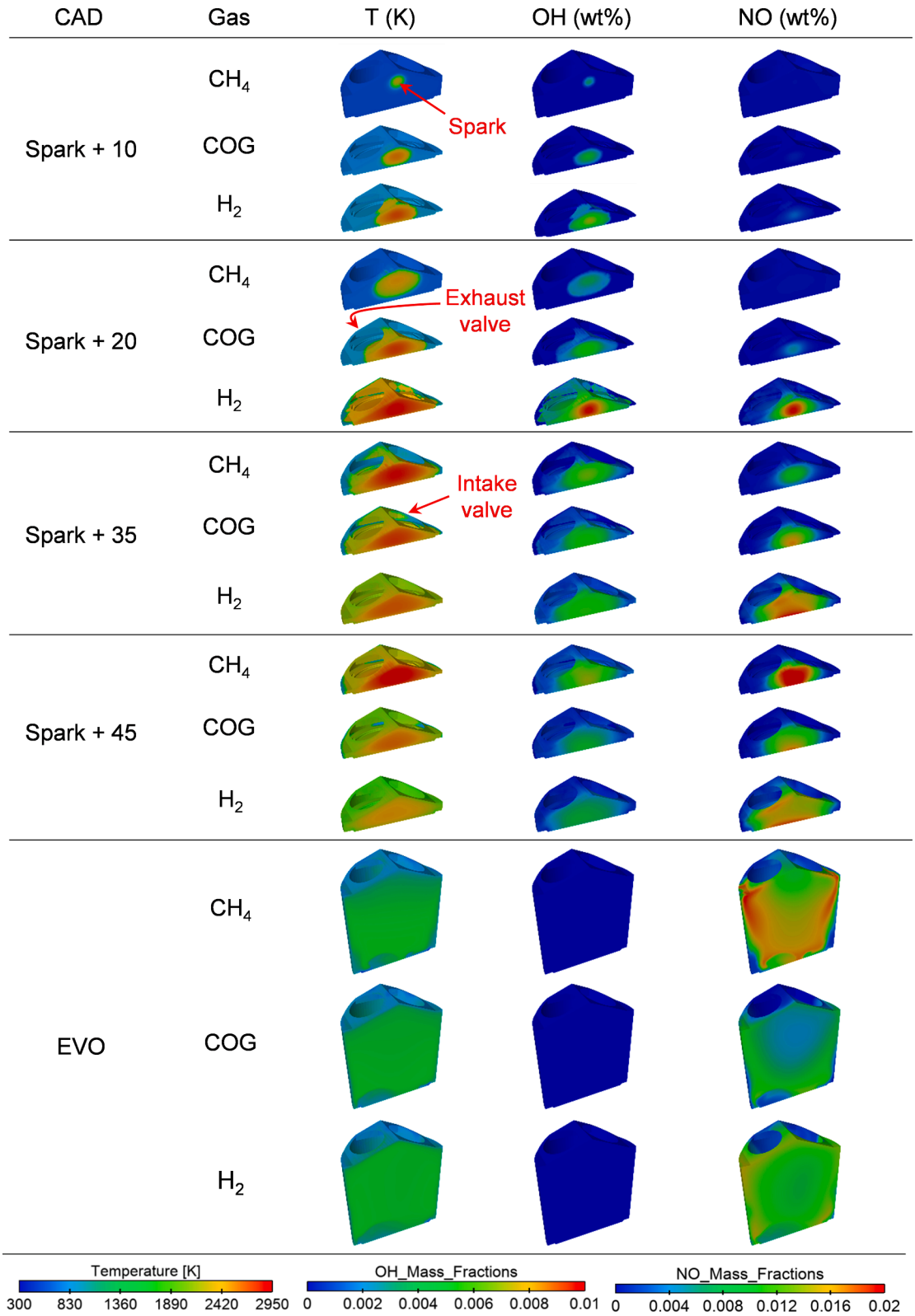

Fig. 6. Temperature (K) and OH and NO mass fraction (wt%) evolution inside the cylinder of CH_4, COG and H_2 at four CAD relative to spark timing and at EVO operating at 4000 rpm and $\lambda = 1.5$. (Screenshots used courtesy of ANSYS, Inc.)

less than CH_4 and 14.3% of WHT less than H_2. Thus, the useful energy released with COG is 16.5% and 5.1% higher than CH_4 and H_2 for that case, respectively. On the other hand, CH_4 is the fuel with the highest heat loss through the cylinder walls at $\lambda = 1.5$ due to the high temperature maintained for longer time, decreasing the resulting brake power.

With lean mixtures ($\lambda = 2$), COG and H_2 release similar chemical heat (Fig. 4c). However, as the model predicts higher heat loss through the walls with COG than with H_2 due to a higher peak temperature during longer time, the useful heat release of COG decreases. In consequence, the simulated brake power of COG is reduced.

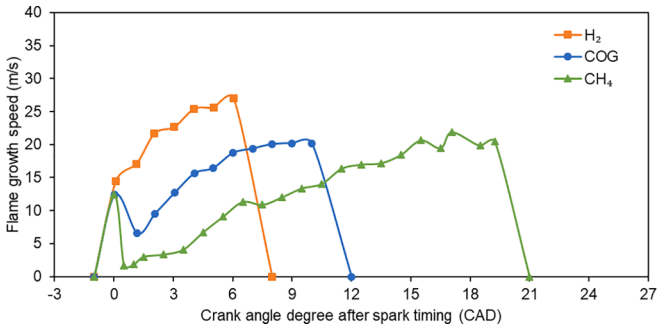

Fig. 7. Flame growth speed (m/s) versus crank angle degree after spark timing (CAD) of H_2 (orange), COG (blue) and CH_4 (green) at 4000 rpm and $\lambda = 1.5$. (For interpretation of the references to colour in this figure legend, the reader is referred to the web version of this article.)

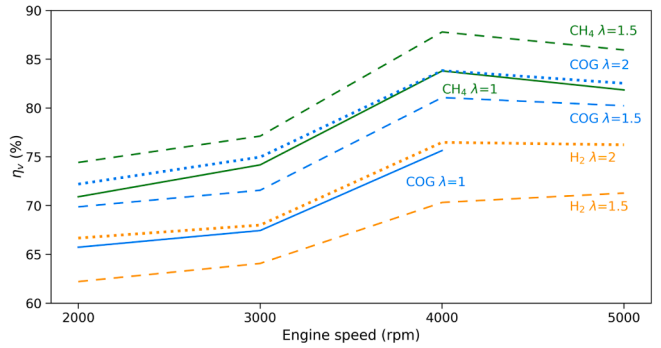

Fig. 8. Volumetric efficiency of H_2 (orange), CH_4 (green) and COG (blue) at $\lambda = 1$ (solid lines), $\lambda = 1.5$ (dashed lines) and $\lambda = 2$ (dotted lines) versus engine speed. (For interpretation of the references to colour in this figure legend, the reader is referred to the web version of this article.)

Regarding the engine speed, operating at higher values, the power increases for all the gaseous fuels because a higher amount of total mass is dragged into the cylinder. However, in the case of CH_4, the model predicts that the intake flow is choked at 5000 rpm, resulting in a lower increment in the power performance than the real values obtained through experiments. A deviation between experimental and simulated power value of 16% for CH_4 and $\lambda = 1$ at 5000 rpm is produced, while the deviation is 15.1% at $\lambda = 1.5$ and same engine speed. This explanation is also valid for COG but with a lower effect due to its intermediate density, with a deviation of 5.8% at 5000 rpm and $\lambda = 1.5$.

3.2. Continuous evolution variables

Ansys® Forte® software allows the tracking of many variables during the simulation at different regions and points of the geometry. In Fig. 5, the average pressure, average temperature and apparent heat release rate (AHRR) inside the cylinder for the three gaseous fuels are graphed during the fourth simulated cycle in the entire speed range (2000–5000 rpm) and all air–fuel ratios: a) $\lambda = 1$, b) $\lambda = 1.5$ and c) $\lambda = 2$. The AHRR (J/CAD) is provided by Forte software as a spatially averaged variable inside the cylinder. It is the result of the difference between the rate of chemical heat release from the combustion reactions and the rate of heat transfer loss through the cylinder walls. Comparing the air-fuel ratio at same engine speed, a clear tendency can be observed, reducing the maximum values as the mixture becomes leaner (higher λ). This is an expected behavior as lower chemical heat release is delivered when the air excess increases with respect to the fuel mass (Fig. 4).

If a comparison between gas fuels is carried out at same λ value, a trade-off between spark advance and H_2 contribution can be highlighted. In the case of $\lambda = 1$, graphed in Fig. 5a, the influence of the contribution of H_2 in the composition of COG is observed in the faster combustion speed due to its higher laminar flame speed, which increases the slope of pressure and temperature curves and the maximum values of temperature and rate of apparent heat release compared to CH_4. In addition, as there is little difference in spark advance between the two gases at the four speeds, low effects on the maximum pressures are derived.

When the air-fuel ratio is 1.5 (Fig. 5b), a smaller difference in the combustion speed is observed between COG and CH_4. However, pure H_2 provides higher laminar flame speed, shortening the combustion duration (see Table S1 in the Supplementary Material) with faster AHRR and delivering the highest temperatures. CH_4 delivers the highest pressure values because the spark is advanced up to 45 CAD between CH_4 and H_2, and up to 35 CAD between CH_4 and COG. However, peak combustion pressure for CH_4 is obtained before TDC at engine speeds higher than 3000 rpm, causing a waste work from the piston to the gas at high pressures at the end of the compression stroke (Fig. 3b). On the other hand, COG and H_2 have close spark timing values, and therefore, similar maximum pressures are achieved. The value of the maximum temperatures and the duration in CAD in which these high values are maintained influence the wall heat transfer, increasing the heat loss as longer and higher peak temperatures are achieved (Fig. 4b).

Therefore, COG benefits from the advantages of both pure fuels. Suitable peak pressures are achieved while lower peak temperatures than CH_4 and H_2 are obtained, reducing the wall heat transfer (Fig. 4b). Therefore, higher power output is achieved with COG, especially at high engine speeds (Fig. 3b).

Finally, in the case of $\lambda = 2$ (Fig. 5c), the laminar flame speed has a

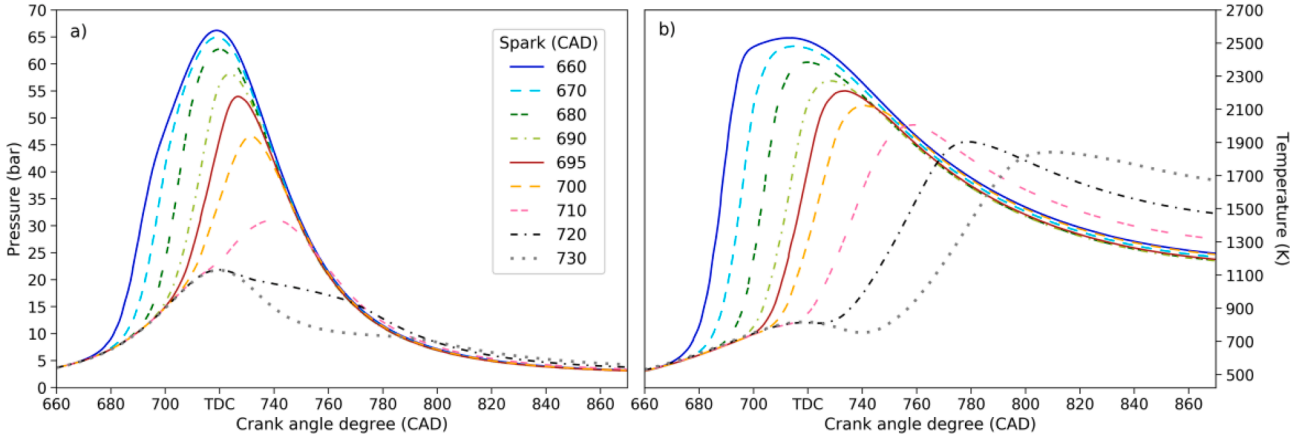

Fig. 9. In-cylinder pressure (a) and temperature (b) for COG at 3000 rpm and $\lambda = 1.5$ at different spark ignition timings.

lower influence with very lean mixtures, reducing the difference in the slope of pressure and temperature between H_2 and COG, and reaching similar maximum values in AHRR. The more advanced spark timing of COG provides higher pressure values (see Fig. 9).

Regarding engine speed, as the rotation speed is increased, the piston displaces at a higher velocity and a greater vacuum is created, inducing a larger mass of air into the cylinder. This phenomenon enables the release of higher chemical energy and power.

The evolution of temperature and mass fraction of OH radical ($OH^{\bullet}$) and NO inside the cylinder of the three gaseous fuels at 4000 rpm and $\lambda = 1.5$ is graphed in Fig. 6 employing the EnSight® module from Ansys®. Four crank angle degrees relative to the spark ignition have been selected to compare the three fuels at the same basis, as the spark ignites at different CAD for each gas (Table 5). Furthermore, the exhaust valve opening (EVO) CAD has been added to see a comparison of the three fuels when the emissions are exhausted. OH is a very interesting radical for the visualization of flame propagation, as it is the most important intermediate product in combustion with a very high activity due to the presence of unpaired electrons [39,69]. Thus, OH reflects the intensity of combustion [70].

As can be observed, the highest laminar flame speed of H_2 (2.65–3.25 m/s, see Table 2) produces the largest temperature core in the spark region at 10 CAD later than spark ignition (Spark + 10 CAD). This generates a higher mass fraction of OH radical where the highest temperature is achieved [39] and a little production of NO. As the CAD progresses, a high mass fraction core of OH and NO are generated in the spark region due to the high combustion intensity [69], with fast decrease as moving away from the flame front. After this, a more homogeneous OH concentration is produced and the NO mass fraction is dispersed along the symmetrical plane with higher concentration in the head and piston areas. Finally, at EVO, a quasi-homogeneous temperature and NO concentration within the cylinder are achieved.

In the case of CH_4, the temperature core due to flame propagation grows slower due to a low laminar flame speed (0.38 m/s), reaching the cylinder walls and generating NO at 35 CAD after spark ignition. Nevertheless, due to the high spark advance (60 CAD before TDC in this case), the very high temperature core is maintained during longer time within the cylinder, increasing NO emissions with a very high concentration mass fraction core of NO in the spark region. At EVO, the NO mass fraction is concentrated heterogeneously, mainly near the cylinder walls and the piston in the central part of the cylinder. Therefore, the high spark advance required for CH_4 at $\lambda = 1.5$ increases notably the NO emissions, reducing its feasibility as clean fuel at lean air-fuel mixtures.

On the other hand, COG, with an intermediate laminar flame speed (0.68–0.88 m/s), generates a core of temperature and OH with a delay with respect to H_2, reaching the cylinder walls in less than 35 CAD after spark ignition. However, the lower maximum values of temperature and OH reached during the combustion (see Fig. 5b) produce lower NO emissions. Therefore, this makes COG an interesting alternative gaseous fuel with the highest performance (Fig. 3b) and lowest NO emissions compared to pure H_2 and pure CH_4 at intermediate air-fuel ratios. Additionally, a sensitivity analysis of the fuel-low content components (CO and CO_2) of COG has been added and explained in the Supplementary Material (Table S4) to analyze their impact on the engine performance and emissions.

In order to provide a further comparison between the fuels, the simulated flame growth speed (m/s), which is the time derivative of the growth of the flame radius, was calculated as the ratio of the increment of the radius (m) and the time elapsed between consecutive simulation steps (s). The resulting flame growth speeds of H_2, COG and CH_4 at 4000 rpm and $\lambda = 1.5$ are graphed in Fig. 7. As can be observed, after a first high increment in the spark radius when it is discharged, the speed of the flame growth increases and reaches a maximum value, as expected in a "spherical" shape flame front and then decreases to zero [71]. Initially, the flame has a spherical shape (as seen with the CH_4 case in Fig. 6), but as the flame increases and reaches the cylinder boundaries, an ellipsoidal shape is adopted (see Fig. S1 in the Supplementary Material).

H_2, with the highest laminar flame speed (Table 2), develops the flame faster and in a shorter time period, increasing the temperature and generating the OH mass fraction at a higher rate than the other two gaseous fuels (Fig. 6). On the other hand, CH_4 has the lowest laminar flame speed and develops the flame at a slower rate, requiring a higher period of crank angle degrees to reach the maximum and then decreases to zero, extinguishing. This can be confirmed with the flame-development angle ($\Delta\theta_d$) from Table S1. (see the Supplementary Material), which describes the CAD between the spark discharges and the release of the 10% of the CHR. COG has an intermediate laminar flame speed but due to the high H_2 percentage, requires less time to reach the maximum spark development before vanishing. Furthermore, a more stable flame development can be observed.

3.3. Volumetric efficiency

In order to study the influence of the gas composition, engine speed and air-fuel ratio variables in the cylinder filling process, the volumetric efficiency (η_v) is graphed in Fig. 8. η_v is defined as the ratio of the actual mass of air introduced in the cylinder and the theoretical mass that would enter at atmospheric conditions (1 atm and 298 K). Hydrogen has the lowest volumetric efficiency because this gas displaces a large amount of incoming air due to its lower density, reducing the available air in the cylinder [72]. In consequence, the mixture mass inside the cylinder is reduced, which decreases the power delivered and CHR (Fig. 3 and Fig. 4). CH_4 has the highest volumetric efficiency due to its higher density. This is confirmed by the experiments carried out with many different fuels by Pourkhesalian et al. [73]. COG, with an intermediate gas density, provides higher volumetric efficiency values than H_2 but lower than CH_4.

Regarding λ, as the mixture becomes leaner, lower fuel is required and a higher amount of air is able to enter into the cylinder, getting closer to the theoretical amount [72]. Finally, as the engine speed rises, the piston increases the vacuum created, which drags a higher amount of air into the cylinder, boosting the volumetric efficiency. In the case of CH_4 and COG, as previously mentioned, the maximum values are obtained at 4000 rpm because at higher engine speed, the intake flow becomes choked, limiting the air flow and reducing the volumetric efficiency due to higher pressure loss [73,74]. In the case of H_2, this effect is delayed to higher engine speeds because the mass of air induced is reduced due to the lower density of hydrogen.

A higher leap in the cylinder mass is observed between 3000 rpm and 4000 rpm than for the rest of the engine speeds for all the gases and air-fuel ratios. This effect is a consequence of the wave pressures in the manifolds, which are induced by the pressure variation inside the cylinder during the intake and exhaust strokes. Wave pressures inside the manifolds are dependent on the geometry design and the speed, whereas they are independent of the fuel used as can be observed in Figs. S2 and S3 from the Supplementary Material. However, though intake manifold pressure is also independent of λ, the exhaust manifold pressure does depend on the air-fuel ratio and the combustion process, especially at low λ and high engine speeds (Fig. S3).

The manifold wave pressures influence the filling and exhaust processes of the cylinder [75]. In Fig. S4 from the Supplementary Material, the mass flow rates and accumulated mass transport exchange between the cylinder and the manifolds of COG at $\lambda = 2$ and all the engine speeds are explained and graphed. In addition, the mass exchange process is graphed for all the fuels, air-fuel ratios and engine speeds in Fig. S5–S7. Therefore, the engine design should take into account these effects when working with gaseous fuels to optimize the intake and exhaust processes to increase the air-fuel mixture mass inside the cylinder, reduce residual mass fraction and avoid choking. This would increase the power output and the efficiency of the engine.

3.4. Spark advance sensitivity

In addition to the previous comparison assessment carried out for H_2, CH_4 and COG for optimum spark advance, a brief analysis of the impact of spark advance with the model will be carried out to support the aforementioned explanations. Simulations for COG at 3000 rpm and $\lambda = 1.5$ varying the spark advance between 660 CAD to 730 CAD have been done.

Fig. 9 shows the pressure and temperature evolution inside the cylinder for the different spark timings. As can be observed, as the spark is ignited earlier, the maximum values of pressure and temperature increase and are advanced with respect to TDC. However, in the case of spark timing at 660 and 670 CAD, the combustion finishes before TDC, but the pressure still increases further with a different slope due to the compression of the piston up to TDC. As the pressure after combustion inside the cylinder is very high, this increases the required work that the piston must exert to continue compression, decreasing the apparent heat release and the power output. On the other hand, the temperature reaches high values due to combustion and it still increases a little with the piston compression until TDC, decreasing afterward as the piston goes down.

As the spark is delayed, the pressure and temperature combustion peaks are closer or even after TDC, which avoids the waste of useful work on piston compression. Furthermore, the slopes of pressure and temperature tend to decrease, producing lower rates of chemical heat release. However, the total wall heat transfer is reduced because high temperatures are maintained for less time.

In the case of spark timing at 710 CAD, the pressure combustion peak is reached 20 CAD after TDC, when the piston has already started to move down, increasing the available cylinder volume. Thus, the peaks of pressure and temperature are reduced compared to higher SA values. With spark timings of 720 and 730 CAD, combustions are produced because the peak temperatures are greater than the temperatures obtained due to only compression (motoring conditions), which are around 820 K. However, the very high delays cause that the peak pressures from combustion are lower than the pressure inside the cylinder TDC due to gas compression (around 22 bar) because the available volume has increased.

In terms of performance, the spark advance has a high influence on the output variables, such as power and efficiency. The influence of the spark advance on the pressure – volume curve (p – V) (known as indicator diagram) is explained and represented in Fig. S9a from the Supplementary Material for COG at 3000 rpm and $\lambda = 1.5$. In addition, the impact of spark timing in brake power (kW), brake specific fuel consumption (BSFC) (g/kWh) and emissions of CO_2 (%), including the experimental values at 695 CAD is explained and graphed in Fig. S9b. A good agreement between simulation and experimental values at spark timing of 695 CAD were obtained, highlighting the importance of using CFD simulations as a predictive tool for ICE optimization. Furthermore, these simulations enable the prediction of the optimum spark advance to achieve maximum power and efficiency for the different fuels and operating conditions, reducing expenditures during engine experiments.

4. Conclusions

In this work the assessment of the engine performance and combustion of low-carbon fuels, H_2, CH_4 and COG, has been carried out through CFD software simulation in terms of pressure, temperature, heat release, emissions, flame growth speed and volumetric efficiency. A CFD model of a symmetrical single cylinder from a naturally-aspirated port-fuel injection Volkswagen Polo 1.4L spark ignition engine has been developed. Simulations of H_2, CH_4 and COG at the experimental operating conditions detailed in Ortiz-Imedio et al. [23] were carried out with Ansys® Forte®. Engine speed was varied in the range 2000–5000 rpm range and with λ between 1 and 2 at full load (WOT) and optimal spark advance. In addition, a spark advance sensitivity analysis has been done for COG. A good agreement between simulations and experiments was achieved, with a weighted standard deviation lower than 12% for power and BMEP variables and 16.3% for thermal efficiency.

Leaner mixtures reduce the pressure and temperature inside the cylinder, as well as the chemical heat release and wall heat transfer, decreasing also NO emissions. OH• radical and NO compound are mainly generated in the hot core of the flame, reducing the concentration as moving away from the spark location.

Spark timing plays a key role, increasing the maximum value of pressure and temperature inside the cylinder and the chemical heat release rate operating at higher spark advances. However, higher wall heat transfer reduces the brake power.

Comparing the fuels at intermediate air-fuel ratios ($\lambda = 1.5$), COG delivers the greatest power output due to a higher flame growth speed than CH_4 and higher volumetric LHV than H_2. Therefore, the intermediate spark advance reduces the maximum temperature and pressure within the cylinder, decreasing the wall heat transfer and the NO emissions. For instance, COG releases up to 40.1% and 14.3% of WHT less than CH_4 and H_2 at 5000 rpm, increasing the apparent heat release around 16.5% and 5.1%, respectively. In addition, the high volumetric H_2 percentage in the COG composition reduces the CO_2 emissions compared to CH_4.

H_2 gaseous fuel, with the highest flame growth speed, reduces the combustion duration but increases the OH generation rate and the total NO emissions. On the other hand, CH_4, due to the lowest flame growth speed, requires very high spark advance values, increasing the maximum pressure and temperature inside the cylinder and maintaining the high values during a longer period of time. Thus, the wall heat transfer and the NO emissions increase with CH_4 compared to the other gaseous fuels.

At richer and leaner mixtures ($\lambda = 1$ and $\lambda = 2$), similar performances are obtained with COG compared to CH_4 and H_2, combining advantages of both pure fuels and widening the air-fuel operation range without abnormal combustion. Therefore, COG offers a very good fuel alternative to H_2 and CH_4 in terms of performance and emissions. Furthermore, COG comes from an industrial waste stream, thus, offering a very interesting fuel valorization alternative for stationary applications with the previous optimization of the operating condition.

Declaration of Competing Interest

The authors declare that they have no known competing financial interests or personal relationships that could have appeared to influence the work reported in this paper.

Acknowledgements

This research was supported by the Project, "HYLANTIC"-EAPA_204/2016, co-financed by the European Regional Development Fund within the framework of the Interreg Atlantic program and the Spanish Ministry of Science, Innovation and Universities (Project: RTI2018-093310-B-I00). Rafael Ortiz-Imedio thanks the Concepción Arenal postgraduate research grant from the University of Cantabria.

The authors acknowledge Santander Supercomputación support group at the University of Cantabria who provided access to the supercomputer Altamira Supercomputer at the Institute of Physics of Cantabria (IFCA-CSIC), member of the Spanish Supercomputing Network, for performing simulations. The authors also acknowledge the help provided for the model development by the Engineering Department from the Public University of Navarre in Pamplona.

Appendix A. Validation results

Validation of the simulations has been carried out through a parity graph between the experiments and simulation results of brake mean effective pressure for the three gaseous fuels and working conditions (Fig. A1). A good agreement can be noticed, with nearly all the points falling in the region between the 15% deviation lines.

In addition, the CO_2 emissions (%vol) have been validated in Fig. A2 for COG and CH_4 in the entire range of study. Higher deviations in the case of CH_4 with leaner mixtures ($\lambda = 1.5$) are observed due to a less stable combustion, increasing the difference between the experiments and the model prediction.

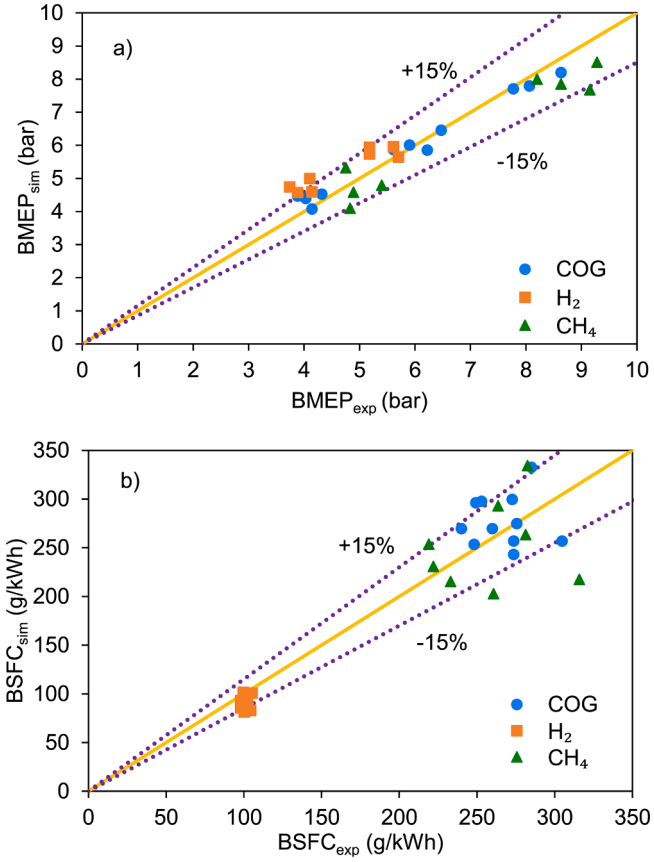

Fig. A1. Parity graph of experimental and simulated results of a) BMEP (bar) and b) BSFC (g/kWh) for COG (●), H_2 (■) and CH_4 (▲) at all operating conditions. Purple dotted lines represent deviation of 15%.

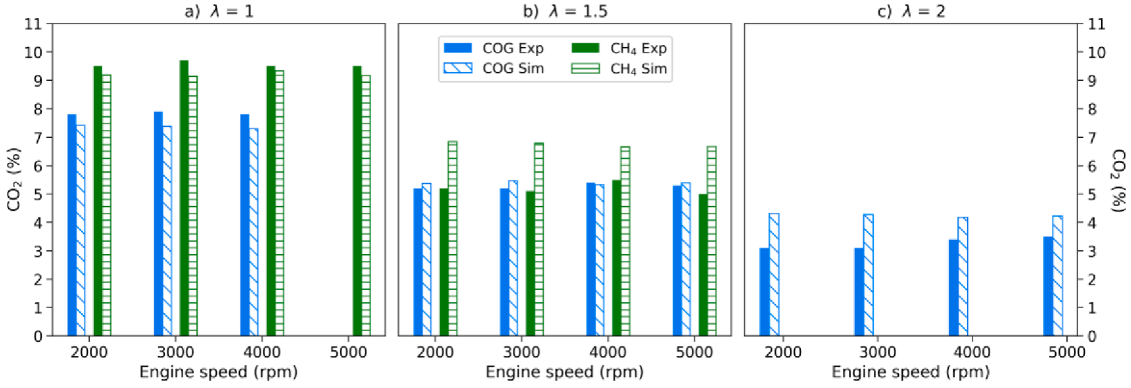

Fig. A2. Experimental and simulated CO_2 emissions (%vol) of COG and CH_4 versus engine speed (rpm) at a) $\lambda = 1$, b) $\lambda = 1.5$ and c) $\lambda = 2$.

Table A1
Weighted standard deviation (σ_w) for some of the experimental variables.

Variable	BMEP (bar)	Power (kW)	η_t (%)	BSFC (g/kWh)	BSEC (MJ/kWh)
σ_w	11.4 %	11.4 %	16.3 %	14.2 %	14.2 %

Furthermore, the statistical parameter weighted standard deviation (σ_w) defined in Eq. (A.1) has been calculated for some of the variables, comparing the experimental and simulated values.

$$\sigma_w = \sqrt{\frac{\sum_{i=1}^{S}\left(\frac{exp-sim}{exp}\right)^2}{S-1}} \tag{A1}$$

Where S is the number of experiments and "exp" and "*sim*" are the experimental and simulated values of each variable, respectively. These σ_w calculated values have been collected in Table A1, in which η_t is the thermal efficiency (%), BSFC is the brake specific fuel consumption (g/kWh) and BSEC is the brake specific energy consumption (MJ/kWh). A deviation lower than 15% for the performance variables is found, with the exception of the thermal efficiency (η_t), increasing up to 16.3%. In the first case, an overestimation of the thermal efficiency is produced at low engine speeds because the model predicts a lower fuel consumption than in the experiments. On the contrary, an underestimation in η_t occurs at high engine speeds because the model assumes the engine consumes more fuel than the required in the experiments and a lower performance is obtained at those engine speeds.

Appendix B. Supplementary data

Supplementary data to this article can be found online at https://doi.org/10.1016/j.enconman.2021.114918.

References

[1] Zhen X, Wang Y, Liu D. Bio-butanol as a new generation of clean alternative fuel for SI (spark ignition) and CI (compression ignition) engines. Renew Energy 2020;147:2494–521. https://doi.org/10.1016/j.renene.2019.10.119.

[2] Ghadikolaei MA, Wong PK, Cheung CS, Ning Z, Yung K-F, Zhao J, et al. Impact of lower and higher alcohols on the physicochemical properties of particulate matter from diesel engines: A review. Renew Sustain Energy Rev 2021;143:110970. https://doi.org/10.1016/j.rser.2021.110970.

[3] Pan S, Li X, Han W, Huang Y. An experimental investigation on multi-cylinder RCCI engine fueled with 2-butanol/diesel. Energy Convers Manag 2017;154:92–101. https://doi.org/10.1016/J.ENCONMAN.2017.10.047.

[4] Pan S, Cai K, Cai M, Du C, Li X, Han W, et al. Experimental study on the cyclic variations of ethanol/diesel reactivity controlled compression ignition (RCCI) combustion in a heavy-duty diesel engine. Energy 2021;237:121614. https://doi.org/10.1016/j.energy.2021.121614.

[5] Shrivastava K, Thipse SS, Patil ID. Optimization of diesel engine performance and emission parameters of Karanja biodiesel-ethanol-diesel blends at optimized operating conditions. Fuel 2021;293:120451. https://doi.org/10.1016/j.fuel.2021.120451.

[6] White C, Steeper R, Lutz A. The hydrogen-fueled internal combustion engine: a technical review. Int J Hydrogen Energy 2006;31(10):1292–305. https://doi.org/10.1016/j.ijhydene.2005.12.001.

[7] Verhelst S, Wallner T. Hydrogen-fueled internal combustion engines. Prog Energy Combust Sci 2009;35(6):490–527. https://doi.org/10.1016/j.pecs.2009.08.001.

[8] Escalante Soberanis MA, Fernandez AM. A review on the technical adaptations for internal combustion engines to operate with gas/hydrogen mixtures. Int J Hydrogen Energy 2010;35(21):12134–40. https://doi.org/10.1016/j.ijhydene.2009.09.070.

[9] Gonca G, Cakir M, Sahin B. Performance Characteristics and Emission Formations of a Spark Ignition (SI) Engine Fueled with Different Gaseous Fuels. Arab J Sci Eng 2018;43(9):4487–99. https://doi.org/10.1007/s13369-017-2906-3.

[10] Diéguez PM, Urroz JC, Sáinz D, Machin J, Arana M, Gandía LM. Characterization of combustion anomalies in a hydrogen-fueled 1.4 L commercial spark-ignition engine by means of in-cylinder pressure, block-engine vibration, and acoustic measurements. Energy Convers Manag 2018;172:67–80. https://doi.org/10.1016/j.enconman.2018.06.115.

[11] Verhelst S, Sierens R, Verstraeten S. A critical review of experimental research on hydrogen fueled SI engines. SAE Tech Pap 2006. https://doi.org/10.4271/2006-01-0430.

[12] Masuk NI, Mostakim K, Kanka SD. Performance and Emission Characteristic Analysis of a Gasoline Engine Utilizing Different Types of Alternative Fuels: A Comprehensive Review. Energy Fuels 2021;35(6):4644–69. https://doi.org/10.1021/acs.energyfuels.0c04112.

[13] Chen H, He J, Zhong X. Engine combustion and emission fuelled with natural gas: A review. J Energy Inst 2019;92(4):1123–36. https://doi.org/10.1016/j.joei.2018.06.005.

[14] Luo S, Ma F, Mehra RK, Huang Z. Deep insights of HCNG engine research in China. Fuel 2020;263:116612. https://doi.org/10.1016/j.fuel.2019.116612.

[15] Park C, Kim C, Choi Y, Won S, Moriyoshi Y. The influences of hydrogen on the performance and emission characteristics of a heavy duty natural gas engine. Int J Hydrogen Energy 2011;36(5):3739–45. https://doi.org/10.1016/j.ijhydene.2010.12.021.

[16] Diéguez PM, Urroz JC, Marcelino-Sádaba S, Pérez-Ezcurdia A, Benito-Amurrio M, Sáinz D, et al. Experimental study of the performance and emission characteristics of an adapted commercial four-cylinder spark ignition engine running on hydrogen-methane mixtures. Appl Energy 2014;113:1068–76. https://doi.org/10.1016/j.apenergy.2013.08.063.

[17] Mehra RK, Duan H, Juknelevičius R, Ma F, Li J. Progress in hydrogen enriched compressed natural gas (HCNG) internal combustion engines – A comprehensive review. Renew Sustain Energy Rev 2017;80:1458–98. https://doi.org/10.1016/j.rser.2017.05.061.

[18] Yan F, Xu L, Wang Y. Application of hydrogen enriched natural gas in spark ignition IC engines: from fundamental fuel properties to engine performances and emissions. Renew Sustain Energy Rev 2018;82:1457–88. https://doi.org/10.1016/j.rser.2017.05.227.

[19] Alrazen HA, Ahmad KA. HCNG fueled spark-ignition (SI) engine with its effects on performance and emissions. Renew Sustain Energy Rev 2018;82:324–42. https://doi.org/10.1016/j.rser.2017.09.035.

[20] Ma F, Wang Y, Liu H, Li Y, Wang J, Zhao S. Experimental study on thermal efficiency and emission characteristics of a lean burn hydrogen enriched natural gas engine. Int J Hydrogen Energy 2007;32(18):5067–75. https://doi.org/10.1016/j.ijhydene.2007.07.048.

[21] Ball M, Wietschel M. The Hydrogen Economy. Opportunities and Challenges. New York: Cambridge University Press; 2009.

[22] Remus R, Aguado Monsonet MA, Roudier S, Sancho LD. Best Available Techniques (BAT) Reference Document for Iron and Steel Production. vol. BREF-IS. 2013. https://doi.org/10.2791/97469.

[23] Ortiz-Imedio R, Ortiz A, Urroz JC, Diéguez PM, Gorri D, Gandía LM, et al. Comparative performance of coke oven gas, hydrogen and methane in a spark ignition engine. Int J Hydrogen Energy 2021;46(33):17572–86. https://doi.org/10.1016/j.ijhydene.2019.12.165.

[24] Azimov U, Tomita E, Kawahara N, Harada Y. Effect of syngas composition on combustion and exhaust emission characteristics in a pilot-ignited dual-fuel engine operated in PREMIER combustion mode. Int J Hydrogen Energy 2011;36(18):11985–96. https://doi.org/10.1016/j.ijhydene.2011.04.192.

[25] Naeve N, He Y, Deng J, Wang M, Ma F. Waste Coke Oven Gas Used as a Potential Fuel for Engines. SAE Tech Pap 2011;2011-01–09. doi:10.4271/2011-01-0920.

[26] Szwaja S. Dilution of fresh charge for reducing combustion knock in the internal combustion engine fueled with hydrogen rich gases. Int J Hydrogen Energy 2019;44(34):19017–25. https://doi.org/10.1016/j.ijhydene.2018.10.134.

[27] Heywood JB. Internal Combustion Engine Fundamentals. New York: McGraw-Hill Education; 2018.

[28] Karim G. Hydrogen as a spark ignition engine fuel. Int J Hydrogen Energy 2003;28(5):569–77. https://doi.org/10.1016/S0360-3199(02)00150-7.

[29] Corporation USS. Clean Coke Oven Gas. Safety Data Sheet (SDS). Exposure 2010;82493:1–8.

[30] Wang JinHua, Wei ZhiLong, Zhang M, Huang ZuoHua. A review of engine application and fundamental study on turbulent premixed combustion of hydrogen enriched natural gas. Sci China Technol Sci 2014;57(3):445–51. https://doi.org/10.1007/s11431-014-5471-y.

[31] Feng H, Zhang W, Zhang J, Wang X, Zhang X. Availability analysis of a coke oven gas fueled spark ignition engine. Int J Hydrogen Energy 2018;43(3):1835–45. https://doi.org/10.1016/j.ijhydene.2017.11.125.

[32] Liu G, Zhou J, Wang Z, Liu J. Study of Laminar Flame Speeds of Premixed Coke Oven Gas Flame Using Kinetic Simulation. 11th China-Japan-Korea Student Symp. Hangzhou 2017.

[33] D. McNaught A, Wilkinson A. IUPAC Compendium of Chemical Terminology. Gold Book. 2nd ed. 1997.

[34] Gerke U. Numerical analysis of mixture formation and combustion in a hydrogen direct-injection internal combustion engine. PhD Thesis. ETH Zürich 2007.

[35] Knop V, Benkenida A, Jay S, Colin O. Modelling of combustion and nitrogen oxide formation in hydrogen-fuelled internal combustion engines within a 3D CFD code. Int J Hydrogen Energy 2008;33(19):5083–97. https://doi.org/10.1016/j.ijhydene.2008.06.027.

[36] Messner D, Wimmer A, Gerke U, Gerbig F. Application and validation of the 3D CFD method for a hydrogen fueled IC engine with internal mixture formation. SAE Tech Pap 2006;2006. doi:10.4271/2006-01-0448.
[37] Yang Z, Zhang F, Wang L, Wang K, Zhang D. Effects of injection mode on the mixture formation and combustion performance of the hydrogen internal combustion engine. Energy 2018;147:715–28. https://doi.org/10.1016/j.energy.2018.01.068.
[38] Kosmadakis GM, Rakopoulos CD, Demuynck J, De Paepe M, Verhelst S. CFD modeling and experimental study of combustion and nitric oxide emissions in hydrogen-fueled spark-ignition engine operating in a very wide range of EGR rates. Int J Hydrogen Energy 2012;37(14):10917–34. https://doi.org/10.1016/j.ijhydene.2012.04.067.
[39] Duan J, liu F, Yang Z, Sun B, Chen W, Wang L. Study on the NOx emissions mechanism of an HICE under high load. Int J Hydrogen Energy 2017;42(34):22027–35. https://doi.org/10.1016/j.ijhydene.2017.07.048.
[40] Liu X, Liu F, Zhou L, Sun B, Schock H. Backfire prediction in a manifold injection hydrogen internal combustion engine. Int J Hydrogen Energy 2008;33(14):3847–55. https://doi.org/10.1016/j.ijhydene.2008.04.051.
[41] Duan J, Liu F, Sun B. Backfire control and power enhancement of a hydrogen internal combustion engine. Int J Hydrogen Energy 2014;39(9):4581–9. https://doi.org/10.1016/j.ijhydene.2013.12.175.
[42] Subramanian KA, Salvi BL. A Numerical Simulation of Analysis of Backfiring Phenomena in a Hydrogen-Fueled Spark Ignition Engine. J Eng Gas Turbines Power 2016;138:1–10. https://doi.org/10.1115/1.4033182.
[43] Chintala V, Subramanian KA. A CFD (computational fluid dynamics) study for optimization of gas injector orientation for performance improvement of a dual-fuel diesel engine. Energy 2013;57:709–21. https://doi.org/10.1016/j.energy.2013.06.009.
[44] Zhu H, Duan J. Research on emission characteristics of hydrogen fuel internal combustion engine based on more detailed mechanism. Int J Hydrogen Energy 2019;44(11):5592–8. https://doi.org/10.1016/j.ijhydene.2018.08.044.
[45] Duan J, Wu P, Zhu H, Qin G, Wei W. Simplification and applicability studies of a hydrogen-air detailed reaction mechanism. Int J Hydrogen Energy 2019;44(11):5538–42. https://doi.org/10.1016/j.ijhydene.2018.09.173.
[46] Shu J, Fu J, Zhang Y, Xie M, Liu J, Liu J, et al. Influences of natural gas energy fraction on combustion and emission characteristics of a diesel pilot ignition natural gas engine based on a reduced chemical kinetic model. Fuel 2020;261:116432. https://doi.org/10.1016/j.fuel.2019.116432.
[47] De Robbio R, Cameretti MC, Tuccillo R. Ignition and combustion modelling in a dual fuel diesel engine. Propuls Power Res 2020;9(2):116–31. https://doi.org/10.1016/j.jppr.2020.02.001.
[48] Dai X(, Singh S, Krishnan SR, Srinivasan KK. Numerical study of combustion characteristics and emissions of a diesel–methane dual-fuel engine for a wide range of injection timings. Int J Engine Res 2020;21(5):781–93. https://doi.org/10.1177/1468087418783637.
[49] Yousefzadeh A, Jahanian O. Using detailed chemical kinetics 3D-CFD model to investigate combustion phase of a CNG-HCCI engine according to control strategy requirements. Energy Convers Manag 2017;133:524–34. https://doi.org/10.1016/j.enconman.2016.10.072.
[50] Poorghasemi K, Saray RK, Bahlouli K, Zehni A. 3D CFD simulation of a natural gas fueled HCCI engine with employing a reduced mechanism. Fuel 2016;182:816–30. https://doi.org/10.1016/j.fuel.2016.06.005.
[51] Baratta M, Misul D, Xu J. Development and application of a method for characterizing mixture formation in a port-injection natural gas engine. Energy Convers Manag 2021;227:113595. https://doi.org/10.1016/j.enconman.2020.113595.
[52] Zhang S, Li Y, Wang S, Zeng H, Liu J, Duan X, et al. Experimental and numerical study the effect of EGR strategies on in-cylinder flow, combustion and emissions characteristics in a heavy-duty higher CR lean-burn NGSI engine coupled with detail combustion mechanism. Fuel 2020;276:118082. https://doi.org/10.1016/j.fuel.2020.118082.
[53] Pan K, Wallace J. Computational studies of fuel injection strategies on natural gas combustion characteristics in direct-injection engines. Fuel 2021;288:119823. https://doi.org/10.1016/j.fuel.2020.119823.
[54] Kosmadakis GM, Rakopoulos DC, Rakopoulos CD. Assessing the cyclic-variability of spark-ignition engine running on methane-hydrogen blends with high hydrogen contents of up to 50%. Int J Hydrogen Energy 2021;46(34):17955–68. https://doi.org/10.1016/j.ijhydene.2021.02.158.
[55] Zaker K, Askari MH, Jazayeri A, Ebrahimi R, Zaker B, Ashjaee M. Open cycle CFD investigation of SI engine fueled with hydrogen/methane blends using detailed kinetic mechanism. Int J Hydrogen Energy 2015;40(40):14006–19. https://doi.org/10.1016/j.ijhydene.2015.08.040.
[56] Gharehghani A, Hosseini R, Mirsalim M, Yusaf TF. A computational study of operating range extension in a natural gas SI engine with the use of hydrogen. Int J Hydrogen Energy 2015;40:5966–75. https://doi.org/10.1016/j.ijhydene.2015.03.015.
[57] Zaichenko VM, Kiverin AD, Smygalina AE, Tsyplakov AI. Combustion of Lean Hydrogen-Based Mixtures in a Spark Ignition Engine. Therm Eng 2018;65(13):1009–18. https://doi.org/10.1134/S0040601518130141.
[58] Laget O, Richard S, Serrano D, Soleri D. Combining experimental and numerical investigations to explore the potential of downsized engines operating with methane/hydrogen blends. Int J Hydrogen Energy 2012;37(15):11514–30. https://doi.org/10.1016/j.ijhydene.2012.03.153.
[59] He H, Yao D, Wu F. A reduced and optimized kinetic mechanism for coke oven gas as a clean alternative vehicle fuel. J Zhejiang Univ A 2017;18:511–30. doi:10.1631/jzus.A1600636.
[60] Stylianidis N, Azimov U, Maheri A, Tomita E, Kawahara N. Chemical kinetics and CFD analysis of supercharged micro-pilot ignited dual-fuel engine combustion of syngas. Fuel 2017;203:591–606. https://doi.org/10.1016/j.fuel.2017.04.125.
[61] Sopena C, Diéguez PM, Sáinz D, Urroz JC, Guelbenzu E, Gandía LM. Conversion of a commercial spark ignition engine to run on hydrogen: Performance comparison using hydrogen and gasoline. Int J Hydrogen Energy 2010;35(3):1420–9. https://doi.org/10.1016/j.ijhydene.2009.11.090.
[62] Ansys®. Accelerate your engine combustion CFD with Ansys Forte 2016.
[63] Ansys®. Academic Research Forte, Release 2021 R1, Help System, Forte Theory Manual, Ansys Inc. 2021.
[64] Smith GP, Golden DM, Frenklach M, Moriarty NW, Eiteneer B, Goldenberg M, et al. Gri-Mech 3.0 Mechanism n.d. http://combustion.berkeley.edu/gri-mech/version30/text30.html (accessed June 2, 2021).
[65] Han Z, Reitz RD. Turbulence Modeling of Internal Combustion Engines Using RNG κ-ε Models. Combust Sci Technol 1995;106(4–6):267–95. https://doi.org/10.1080/00102209508907782.
[66] Sierens R. VS. Experimental study of a hydrogen-fueled engine. J Eng Gas Turbines Power 2001;123:211–6. doi:10.1115/1.1339989.
[67] Kamil M, Rahman MM. Performance prediction of spark-ignition engine running on gasoline-hydrogen and methane-hydrogen blends. Appl Energy 2015;158:556–67. https://doi.org/10.1016/j.apenergy.2015.08.041.
[68] Ma F, Wang Yu, Wang J, Ding S, Wang Y, Zhao S. Effects of combustion phasing, combustion duration, and their cyclic variations on spark-ignition (SI) engine efficiency. Energy Fuels 2008;22(5):3022–8. https://doi.org/10.1021/ef8003027.
[69] Wang J, Huang Z, Tang C, Miao H, Wang X. Numerical study of the effect of hydrogen addition on methane-air mixtures combustion. Int J Hydrogen Energy 2009;34(2):1084–96. https://doi.org/10.1016/j.ijhydene.2008.11.010.
[70] Zhu H, Zhang Yu, Liu F, Wei W. Effect of excess hydrogen on hydrogen fueled internal combustion engine under full load. Int J Hydrogen Energy 2020;45(39):20419–25. https://doi.org/10.1016/j.ijhydene.2019.12.022.
[71] Cruccolini V, Discepoli G, Cimarello A, Battistoni M, Mariani F, Grimaldi CN, et al. Lean combustion analysis using a corona discharge igniter in an optical engine fueled with methane and a hydrogen-methane blend. Fuel 2020;259:116290. https://doi.org/10.1016/j.fuel.2019.116290.
[72] Hamada KI, Rahman MM, Ramasamy D, Noor MM, Kadirgama K. Numerical investigation of in-cylinder flow characteristics of hydrogen-fuelled internal combustion engine. J Mech Eng Sci 2016;10(1):1782–802. https://doi.org/10.15282/jmes10.15282/jmes.10.1.2016.4.0172.
[73] Pourkhesalian AM, Shamekhi AH, Salimi F. Alternative fuel and gasoline in an SI engine: A comparative study of performance and emissions characteristics. Fuel 2010;89(5):1056–63. https://doi.org/10.1016/j.fuel.2009.11.025.
[74] Rahman MM, K. Mohamme M, A. Bakar R. Effects of Air-Fuel Ratio and Engine Speed on Performance of Hydrogen Fueled Port Injection Engine. J Appl Sci 2009;9(6):1128–34. https://doi.org/10.3923/jas.2009.1128.1134.
[75] Duan X, Liu Y, Liu J, Lai M-C, Jansons M, Guo G, et al. Experimental and numerical investigation of the effects of low-pressure, high-pressure and internal EGR configurations on the performance, combustion and emission characteristics in a hydrogen-enriched heavy-duty lean-burn natural gas SI engine. Energy Convers Manag 2019;195:1319–33. https://doi.org/10.1016/j.enconman.2019.05.059.
[76] Academic Research Forte Ansys®. Release 2021 R1, Help System. Forte User's Guide, Ansys Inc; 2021.
[77] Sáinz Casas David. Adaptación de un motor de combustión interna alternativo de gasolina para su funcionamiento con hidrógeno como combustible. Aplicaciones energética y de automoción. PhD thesis. Universidad Pública de Navarra 2014.